Batteries & Supercaps

Research Article
doi.org/10.1002/batt.202500499

Chemistry Europe
European Chemical Societies Publishing

www.batteries-supercaps.org

Simultaneous Top-Down and Bottom-Up Synthesis of Metal-Free g-C_3N_4/Graphene Hybrid via Mechanochemical Exfoliation and Thermal Treatment for High-Performance Supercapacitors

Haritha Valiyaveettil Padi, Vijayasree Haridas, and Binitha N. Narayanan*

A dual synthetic strategy is introduced here for the preparation of a hybrid g-C_3N_4/graphene nanocomposite using a cost-effective ball milling method followed by thermal treatment for supercapacitor applications. Graphite is exfoliated to graphene via a top-down route, where melamine serves as both the milling agent and the precursor for the bottom-up synthesis of g-C_3N_4. This approach integrates both materials efficiently, yielding synergistic properties. The hybrid material delivers an ultrahigh specific capacitance of 1415.7 F g^{-1} at 3 A g^{-1}, with negligible internal resistance, confirming its excellent energy storage performance. Cyclic voltammetry and Dunn's method analysis reveal significant pseudocapacitive contributions to energy storage. A coin cell supercapacitor with the g-C_3N_4/graphene electrodes exhibits an areal capacitance of 222.3 mF cm^{-2} (168.3 F g^{-1}) at 0.1 mA cm^{-2} with an energy density of 13.54 μWh cm^{-2} (23.3 Wh kg^{-1}) and a power density of 5.13 mW cm^{-2} (3885.3 W kg^{-1}). The device, after 10,000 galvanostatic charge-discharge cycles, shows an increase in its activity to 109.9% as a result of the improved diffusion of electrolyte ions over time. A series-connected arrangement of three symmetric supercapacitors is utilized to power a mini fan and illuminate five green LEDs, highlighting the real-world applicability.

1. Introduction

Along with significant depletion, fossil fuels contribute heavily to the carbon footprint, making them unsuitable for a sustainable future.[1–3] This challenge has accelerated the development of clean, sustainable, and portable energy storage systems such as supercapacitors, which are renowned for their superior cycle life, low maintenance, and excellent power density compared to most batteries, whose usage is increasingly limited by growing demands for faster and higher power delivery.[4] Batteries have high energy density, benefiting from a longer energy supply, but fail in quick power delivery in domestic to commercial applications.[5] Conversely, supercapacitors excel in quick power bursts; however, the energy density is yet to reach optimal levels and warrants further improvement.[6] In batteries, the Faradaic charge transfer processes reach up to the bulk of electrodes lead to higher energy density, but solid-state ion diffusion limitations prevent capacity improvement.[7] These Faradaic materials often suffer from poor cyclic stability due to the gradual consumption, degradation, or aggregation of the electrode material during redox reactions.[8] In supercapacitors, energy storage is mediated either by the formation of an electrical double layer at the electrode–electrolyte interface or by the Faradaic charge transfer processes on the surface and immediate bulk (pseudocapacitive charge storage).[9] The surface double-layer-mediated charge storage also offers the added advantage of rapid charge–discharge (CD) capability, high power density, and excellent cycling life.[4,8,9] These aspects substantiate the development of supercapacitors for various energy storage applications with the aim of delivering excellent power density and good energy density.[10–12] A highly promising approach involves developing hybrid supercapacitor electrode materials by combining non-Faradaic materials with those exhibiting Faradaic charge storage, aiming to enhance energy density while retaining the high power density.[13] In this perspective, graphene is an appealing candidate, having a capacitive charge storage mechanism and also acts as the conductive counterpart in these hybrid composites.[14,15] Pristine graphene is a pure electrical double layer capacitor (EDLC) electrode material, on account of which researchers focus on an enormous quest towards the exploitation of graphene-based materials for supercapacitors with promising power density.[16] Rather than pure graphene, its composites with various materials offer improved properties, complementing supercapacitor performance.[16] Among these, studies involving the combination of graphene with other similar 2D materials are emerging nowadays.[17,18]

H. V. Padi, B. N. Narayanan
Department of Chemistry
University of Calicut
Calicut University (P.O.), Thenhipalam, Kerala 673635, India
E-mail: binitha@uoc.ac.in

V. Haridas
Inter University Centre for Nanomaterials and Devices (IUCND)
Cochin University of Science and Technology (CUSAT)
Cochin, Kerala 682022, India

B. N. Narayanan
Inter University Centre for Hydrogen & Energy Storage
University of Calicut
Calicut University (P.O.), Thenhipalam, Kerala 673635, India

Supporting information for this article is available on the WWW under https://doi.org/10.1002/batt.202500499

The common preparation methods for graphene that involve chemical oxidation will reduce the conductivity of graphene owing to their broken aromatic π-network resulting from drastic reaction conditions.[19] Moreover, the hazardous nature of graphene oxide (GO) synthesis and the high cost of less-defective graphene obtained through chemical vapor deposition continue to hinder their widespread applications.[20,21] Mechanical exfoliation of graphite to graphene by ball milling is known to preserve the conducting aromatic π-conjugative network of graphene with the additional advantage of hassle-free introduction of various desirable functional groups at the edges of sheets, as well as heteroatom doping aided by a suitable milling agent, further facilitating its electrochemical performance.[22] The ball milling method is also scalable and environmentally benign, with preferably green milling agents that, upon suitable treatment, produce edge-functionalized graphene from the ball–milled mixture.[23] However, graphene layers tend to restack into the multilayered graphitic structure, which may hinder their EDLC by reducing the surface area and electrolyte accessibility.[24]

To prevent graphene from restacking, various spacer materials can be used, as their molecular adsorption over graphene can decrease the van der Waals attractions between graphite layers.[24,25] 2D materials like exfoliated g-C_3N_4 can act as excellent spacers for graphene due to their similar graphitic microstructure, along with the ability to modify its electrical properties.[24,26] g-C_3N_4 is an artificial polymeric material with an N-atom substituted in the graphite framework, and it has been extensively explored for photocatalytic applications. Bulk g-C_3N_4 has poor electrical properties, yet they are tunable upon layer exfoliation.[27] It has two known basic subunits, namely s-triazine and tri-s-triazine, of which the latter is the most stable.[28] This abundant material, having excellent chemical and thermal stability, can be prepared by thermal polymerization of N-rich precursors like melamine, urea, dicyanodiamide, etc.[29] Its layers consist of triangular nanopores between the tri-s-triazine units, thereby assisting high ion transport rates.[30] Material engineering is also promoted to further expand the electronic properties of this metal-free semiconductor material, such as enhancing the conductivity.[31,32] In contrast to the commonly used metal oxides or conducting polymers, g-C_3N_4 with intrinsic nitrogen functionalities enables effective nitrogen doping over graphene in combination.[33] The nitrogen functionalities in g-C_3N_4 also impart pseudocapacitive characteristics to the hybrid material by exhibiting Faradaic charge storage, where energy storage occurs through redox reactions.[25] The redox-active g-C_3N_4 with exposed nitrogen sites for Faradaic reactions, with its strong synergistic interaction with a highly conductive, high surface area graphene matrix, can enable high specific capacitance.[17,25,34] Compared to conventional methods, the in situ synthesis of g-C_3N_4 on graphene can ensure strong interfacial contact and uniform dispersion, greatly enhancing charge transfer and overall conductivity, which benefits supercapacitor performance.

In the literature, there are only a few reports on metal-free g-C_3N_4/graphene hybrid nanocomposites for supercapacitor applications. Sonkawade et al. reported a combination of g-C_3N_4 and reduced GO (rGO) with a specific capacitance of 407.7 F g^{-1}, with an energy density of 11.4 Wh kg^{-1}, and a power density of 186.7 W kg^{-1}.[35] The nanocomposite retained 83% of its initial capacitance after 5000 galvanostatic charge-discharge (GCD) cycles. Ding et al. prepared an rGO/g-C_3N_4 modified carbon fiber as the electrode for a solid-state supercapacitor, which exhibited an areal capacitance of 61 mF cm^{-2} at 1 mA cm^{-2} and showed 90% capacitance retention after 5000 stability runs.[36] The device displayed an energy density of 8.75 μWh cm^{-2} and a power density of 0.45 mW cm^{-2}. Another work on g-C_3N_4/rGO was reported by Lin et al. where the g-C_3N_4 was oxidized prior to nanocomposite formation.[11] The obtained material has a specific capacitance of 265.6 F g^{-1} at 1 A g^{-1} in the three-electrode configuration and a capacitance retention of 94% over 5000 cycles. A symmetrical device fabricated also showed a specific capacitance of 170.7 F g^{-1} along with an energy density of 7.47 Wh kg^{-1}. Chen et al. prepared a 3D graphene nanocomposite with g-C_3N_4 that had a specific capacitance of 264 F g^{-1} at 0.4 A g^{-1} in the two-electrode system, with an energy density of nearly 30 Wh kg^{-1} and power density of 4.0 kW kg^{-1}.[37] Most of these nanocomposites utilize rGO as the conducting counterpart, which has lower conductivity than pristine graphene. The integration of highly conductive graphene is a better strategy to improve the electrochemical performance of g-C_3N_4-based hybrid supercapacitors.[38] Moreover, in situ formation offers improved structural stability and scalability over the reported post-synthesis mixing strategies.[38,39] The layered structure of the g-C_3N_4/graphene nanocomposite affirms increased surface area, greater ionic conductivity, and ultrahigh specific capacitance due to the mutual synergy, which also assures supercapacitors with promising energy and power densities.[27,40] The features of integral voids in the g-C_3N_4/graphene nanocomposite enable smoother permeation of electrolyte ions, which can complement the excellent supercapacitor activity.[13] This approach also prevents g-C_3N_4 agglomeration and promotes seamless integration with graphene's conductive network.[40] In supercapacitor applications, the resulting nanocomposite leverages the pseudocapacitance of g-C_3N_4 and the electrical double-layer capacitance of graphene for superior performance.

In this work, a novel, simple two-step synthetic procedure involving mechanochemical exfoliation and thermal treatment is used for the in situ preparation of a g-C_3N_4/graphene hybrid nanocomposite. Melamine (2,4,6-triamino-1,3,5-triazine) serves as a milling agent to exfoliate graphite into graphene while partially polymerizing, and upon subsequent heat treatment, it completely transforms into g-C_3N_4 that actively interacts with the exfoliated graphene sheets, producing a g-C_3N_4/graphene nanocomposite via a concurrent top-down and bottom-up approach. Thus, overall, the work depicts a cost-effective, green, and scalable method to produce a promising metal-free g-C_3N_4/graphene nanocomposite for use in the next-generation supercapacitors. Here we have also fabricated a symmetric coin cell supercapacitor that, when connected in series with two similar devices, lit 5 green LEDs and powered a mini-motor-based fan.

2. Results and Discussion

To produce graphene with desired properties, ball milling of graphite employs suitable milling agents that not only overcome

Research Article
doi.org/10.1002/batt.202500499
Chemistry Europe
European Chemical Societies Publishing

the interlayer attraction between graphite sheets but also efficiently introduce edge functionalization or heteroatom doping.[41] During milling, the balls inside the mill exert both shear force and compression force on graphite flakes arising from the oppositely directed movement of the grinding jar and milling balls, causing graphite layer exfoliation.[42,43] Milling agents are adsorbed onto graphite and assist exfoliation by intercalating between the layers. The use of excess milling agent also prevents restacking of graphene sheets and direct hits by balls on graphite.[44] Here, melamine, being an amino triazine derivative, strongly adsorbs onto graphite and generates an assembly over the sheets due to interadsorbate hydrogen bonding, which promotes nanocomposite formation.[30,45–48] Under thermal treatment, melamine condenses to melam with prominent terminal groups.[10,49] Tri-s-triazine units linked by edge -NH_2 groups represents to the most stable form of g-C_3N_4.[45] Through milling, we obtain a mixture of partially condensed g-C_3N_4 and graphene, and further thermal treatment assists in the formation of the remaining g-C_3N_4 that adheres to graphene (Represented in **Figure 1** in the Supporting Information S5).

2.1. Structural Investigation of g-C_3N_4/graphene

The X-ray diffraction (XRD) patterns of the g-C_3N_4/graphene show (002) planes of both g-C_3N_4 and graphene with low intensity at 2θ values of 27.9° and 26.6°, respectively, evidencing excellent layer exfoliation (Figure 1a).[50,51] XRD patterns confirm the co-existence of both the well-exfoliated 2D materials in the nanocomposite.[51]

Fourier transform infrared (FTIR) spectroscopy is a commonly employed technique for characterizing g-C_3N_4-based materials, as they display a distinct set of characteristic peaks within the 1200–1650 cm^{-1} range.[52] The FTIR spectrum of g-C_3N_4/graphene and that of bulk g-C_3N_4 are shown in Figure 1b. The peaks in the range of 1200–1650 cm^{-1} are associated with the stretching vibrations of aromatic heptazine repeating units, including sp^2 C═N stretching modes and out-of-plane bending vibrations of sp^3 C—N bonds of g-C_3N_4.[53] Additionally, peaks at 1205, 1236, and 1313 cm^{-1} correspond to the bridging C—NH—C units.[54] The absorption band at 883 cm^{-1} is attributed to the deformation mode of N—H in amino groups, and the breathing mode of tri-s-triazine cycles is observed at 810 cm^{-1}.[55] In the 3000–3500 cm^{-1} region, the spectra reveal the stretching vibrations of terminal C—NH_2 groups, residual free N—H in bridging C—NH—C units, and O—H stretching from the adsorbed water.[56,57] A blueshift in the NH_2/NH bonding vibrations is observed in g-C_3N_4/graphene compared to bulk g-C_3N_4, indicating the dissociation of some hydrogen bonds, which suggests exfoliation of g-C_3N_4.[54] Furthermore, the intensity of NH_2 and NH bonds is reduced, and their peaks become well-separated in the nanocomposite, providing evidence of interactions between g-C_3N_4 and graphene through weak noncovalent interactions (such as hydrogen bonding through NH_2/NH linkages with the aromatic π-network of graphene).[54,58,59] The aromatic

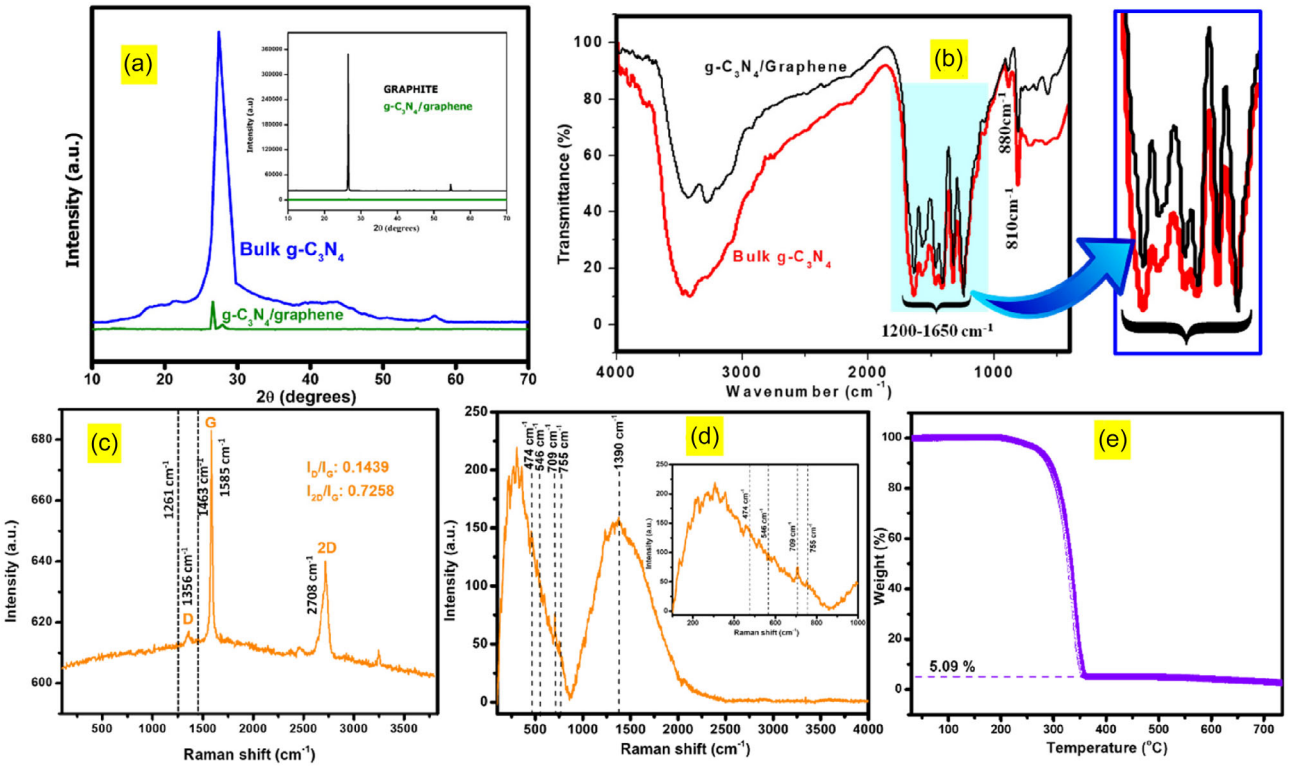

Figure 1. a) XRD patterns of g-C_3N_4/graphene, graphite and bulk g-C_3N_4, b) FTIR spectra of g-C_3N_4/graphene and bulk-g-C_3N_4, c) Raman spectrum of g-C_3N_4/graphene with 532 nm laser, d) with 785 nm laser, and e) TGA of g-C_3N_4/graphene nanocomposite.

region, represented by C=C and C=N bonds, also exhibits slight disturbances, indicative of noncovalent π–π interactions between the exfoliated graphene and g-C_3N_4 sheets. The exfoliation of graphite using melamine via noncovalent interactions has been previously reported, but the milling agent was simply removed by preparing a concentrated dispersion of the graphene–melamine mixture in dimethylformamide (DMF), which was then washed with hot water to remove melamine. Unexfoliated graphite, which settles during the dispersing of the mixture in DMF, was also removed.[47] The obtained graphene was then redispersed in DMF to obtain a stable dispersion.[47] In our approach, instead of being simply discarded, melamine, which was used as the milling agent, was effectively converted into g-C_3N_4 through a thermal treatment, resulting in the in situ preparation of a g-C_3N_4/graphene nanocomposite for the first time via such a simple method.

Raman spectrum of g-C_3N_4 /graphene is shown in Figure 1c. As per the literature, both g-C_3N_4 and graphene have peaks in Raman spectra around 1300 and 1500 cm^{-1}, and hence can undergo spectral merging due to the π–π interactions of the 2D counterparts.[60] The g-C_3N_4/graphene exhibits characteristic peaks at 1356 and 1585 cm^{-1}, corresponding to the D and G bands of graphene, respectively in the 532 nm laser.[60,61] An I_D/I_G ratio of 0.14 indicates minimal structural defects, while the I_{2D}/I_G (0.72) ratio, based on the 2D band observed at 2708 cm^{-1}, confirms the presence of few-layer graphene in the nanocomposite.[62,63] Additional peaks observed at 1261 and 1643 cm^{-1} in the Raman spectra correspond to the CN heterocycles of g-C_3N_4, confirming the presence of g-C_3N_4 in the nanocomposite.[64] Since the characteristic peaks of g-C_3N_4 around 1300 and 1500 cm^{-1} can overlap with the D and G bands of graphene, Raman analysis of g-C_3N_4 /graphene was also performed using a 785 nm laser, as shown in Figure 1d, and the peaks in the range of 400–800 cm^{-1} are given in the inset. In this range, the g-C_3N_4/graphene nanocomposite exhibits distinct peaks at 474, 546, 709, and 755 cm^{-1}, which are characteristic of g-C_3N_4, further confirming the successful incorporation of g-C_3N_4 and the coexistence of both g-C_3N_4 and graphene in the nanocomposite.[64] The intense Raman band around 1390 cm^{-1} corresponds to g-C_3N_4 (Figure 1d).[64,65] The mass loss of the ball–milled mixture during thermal treatment was investigated using the thermogravimetric analysis (TGA) under an N_2 atmosphere (Figure 1e). The initial weight loss up to 200 °C indicates water evaporation, and the major weight loss occurs in the range of 200–360 °C. About 5.09% of its initial weight was retained after 550 °C, where the weight of the graphite taken is only 3.22%. The final retained weight corresponding to the graphene is thus only 3.22% and the additional weight of 1.87% mostly corresponds to the formed g-C_3N_4.

Since g-C_3N_4/graphene is a hybrid material of two distinct layered 2D materials, the morphology and structure were also comprehensively examined using field emission scanning electron microscopy (FESEM) and transmission electron microscopy (TEM) images. The FESEM images show layered stacks over the big sheets as shown in **Figure 2**a–c, suggesting the distribution of g-C_3N_4 over graphene. In the TEM images, the curled nature of the layered material is visible, with few-layer graphene having slightly rolled-up sheet edges as shown in Figure 2d–f.

The energy dispersive X-ray spectroscopy (EDS) elemental mapping of the nanocomposite was performed to understand the elemental composition of g-C_3N_4/graphene. The data showed the presence of carbon and nitrogen in the composite along with a negligible amount of oxygen that can be aroused from adsorbed water or oxygen (**Figure 3**). There is a uniform distribution of carbon and nitrogen in the nanocomposite, indicating the successful formation of a hybrid nanocomposite with effective interaction between the components.

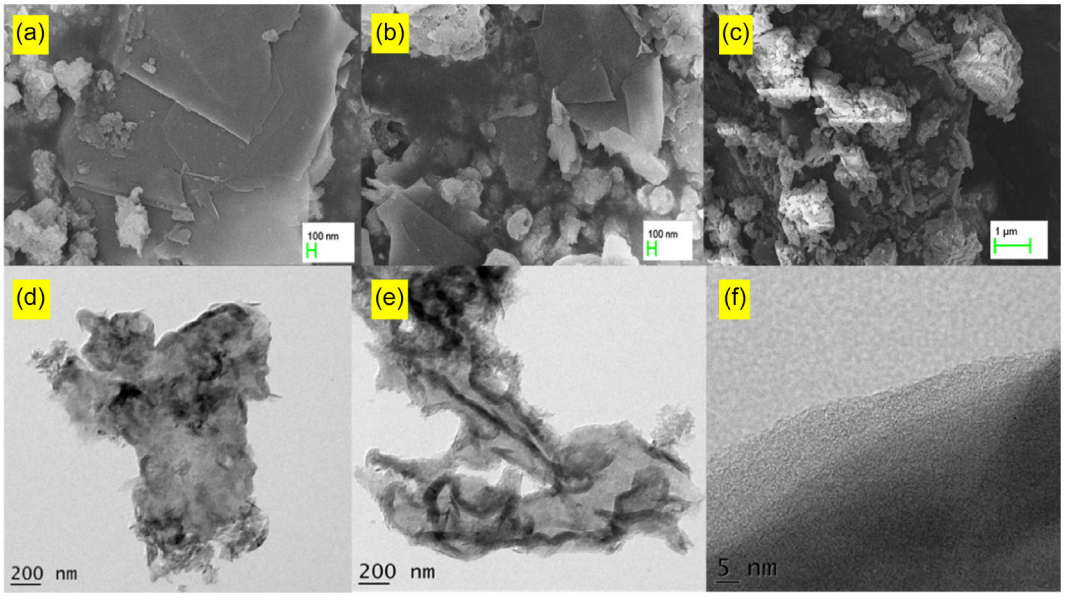

Figure 2. a–c) FESEM images of g-C_3N_4/graphene and d–f) HRTEM images of g-C_3N_4/graphene.

Research Article
doi.org/10.1002/batt.202500499
Chemistry Europe
European Chemical Societies Publishing

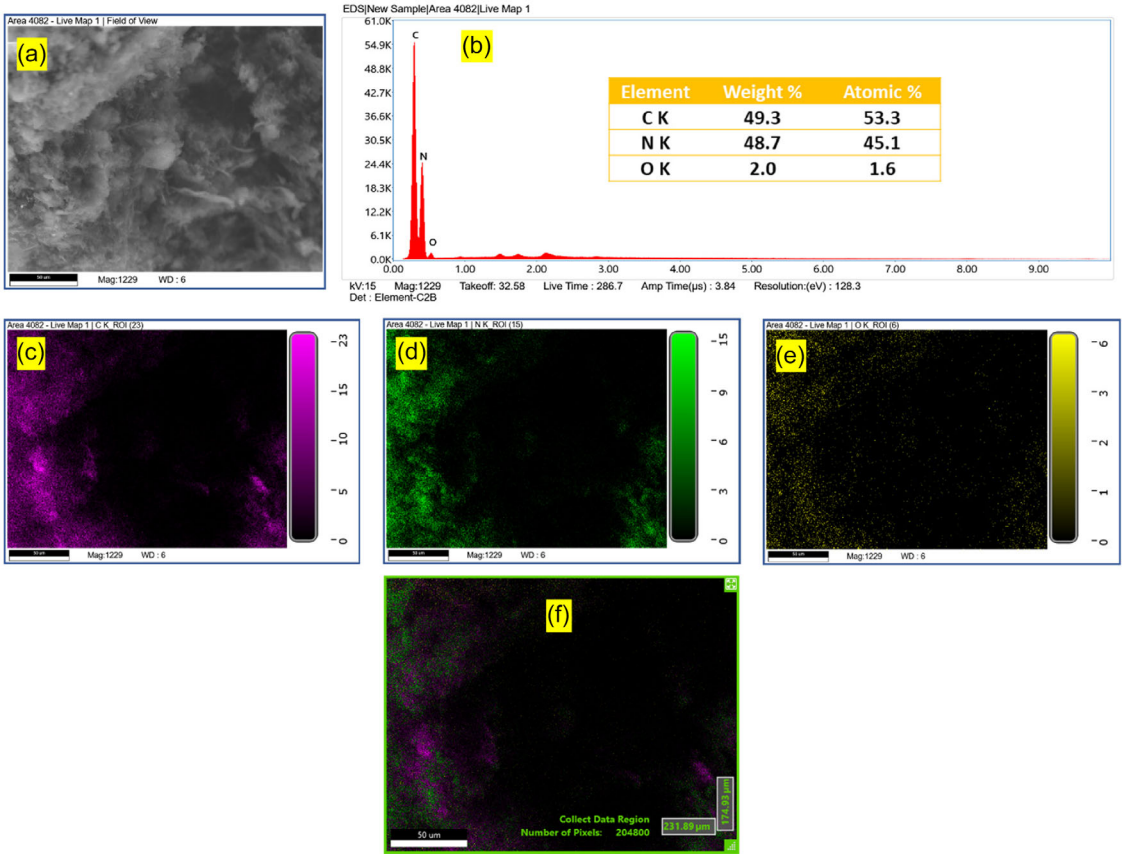

Figure 3. a) Selected area SEM of g-C_3N_4/graphene, b) EDS spectra of g-C_3N_4/graphene, c–e) EDS mapping of different elements of g-C_3N_4/graphene, and f) EDS mapping of g-C_3N_4/graphene at the selected area.

X-ray photoelectron spectroscopy (XPS) was used to investigate the compositional features of g-C_3N_4/graphene and to resolve the interactions between g-C_3N_4 and graphene. The wide scan spectrum unveiled major peaks at 290 eV, 396.6 eV, and 534.6 eV, respectively, corresponding to carbon (C 1*s*), nitrogen (N 1*s*), and oxygen (O 1*s*) (**Figure 4**a).[58,66] All the peaks were then deconvoluted and identified as follows. The C 1*s* peak comprised five deconvoluted component peaks at 284.2, 284.8, 287.7, 288.5, and 290 eV. The peak at 284.2 eV represents the aromatic C═C of graphene, and that at 284.8 eV corresponds to the sp^2 C═N in triazine rings present in g-C_3N_4.[67] The peaks at 287.7 and 288.5 eV arise from C atoms in NC_3 and N—C═N bonds of g-C_3N_4.[68] The π–π interactions common in few-layered materials were reflected by a peak at 290 eV in the deconvoluted peak of C 1*s* (Figure 4b).[69,70]

The N 1*s* spectrum exhibited five deconvoluted peaks at 397.3, 398.6, 399.5, 400.9, and 404.7 eV. The major peak at 398.6 eV denotes the N of C═N—C, and the second largest peak at 399.5 eV represents the ternary N of NC_3.[58,71] The peaks centered around 397.3 and 400.9 eV, respectively, represent C═N bonding interactions of g-C_3N_4 and N involved in the C—N—H interactions (Figure 4c).[72,73] The least prominent O 1*s* peak originates from adsorbed oxygen and adsorbed water, as evident from the deconvoluted O 1*s* peaks around 531.5 and 532.6 eV, respectively (Figure 4d).

Various characterization techniques thus revealed the coexistence and interactions of well-exfoliated g-C_3N_4 and graphene in the nanocomposite, which can deliver excellent supercapacitor performance.

2.2. Electrochemical Evaluation

The supercapacitor activity of the g-C_3N_4/graphene was first evaluated using a three-electrode setup. The cyclic voltammogram (CV) of g-C_3N_4/graphene was compared with that of bulk g-C_3N_4, where the area enclosed within the CV curve of the nanocomposite was much higher than that of bulk g-C_3N_4, revealing the higher specific capacitance of the g-C_3N_4/graphene electrode material. The shape of the CV of g-C_3N_4/graphene was distorted from the rectangular shape, proposing a contribution of pseudocapacitance to the energy storage (**Figure 5**a).[74]

From Figure 5b, the charge discharge (CD) curve of bulk g-C_3N_4 is compared with that of g-C_3N_4/graphene, and the results reaffirm the excellent supercapacitor activity compared to that of bulk g-C_3N_4. The CV curves preserve the shape at varying scan rates, as given in Figure 5c, which refers to the least resistive behavior of g-C_3N_4/graphene, and the current response showcases a gradual rise from lower to higher scan rates, shown by the enhanced area of CV. The nonlinear CD curves exhibit a decrease in specific capacitance values along

Research Article
doi.org/10.1002/batt.202500499
Chemistry Europe
European Chemical Societies Publishing

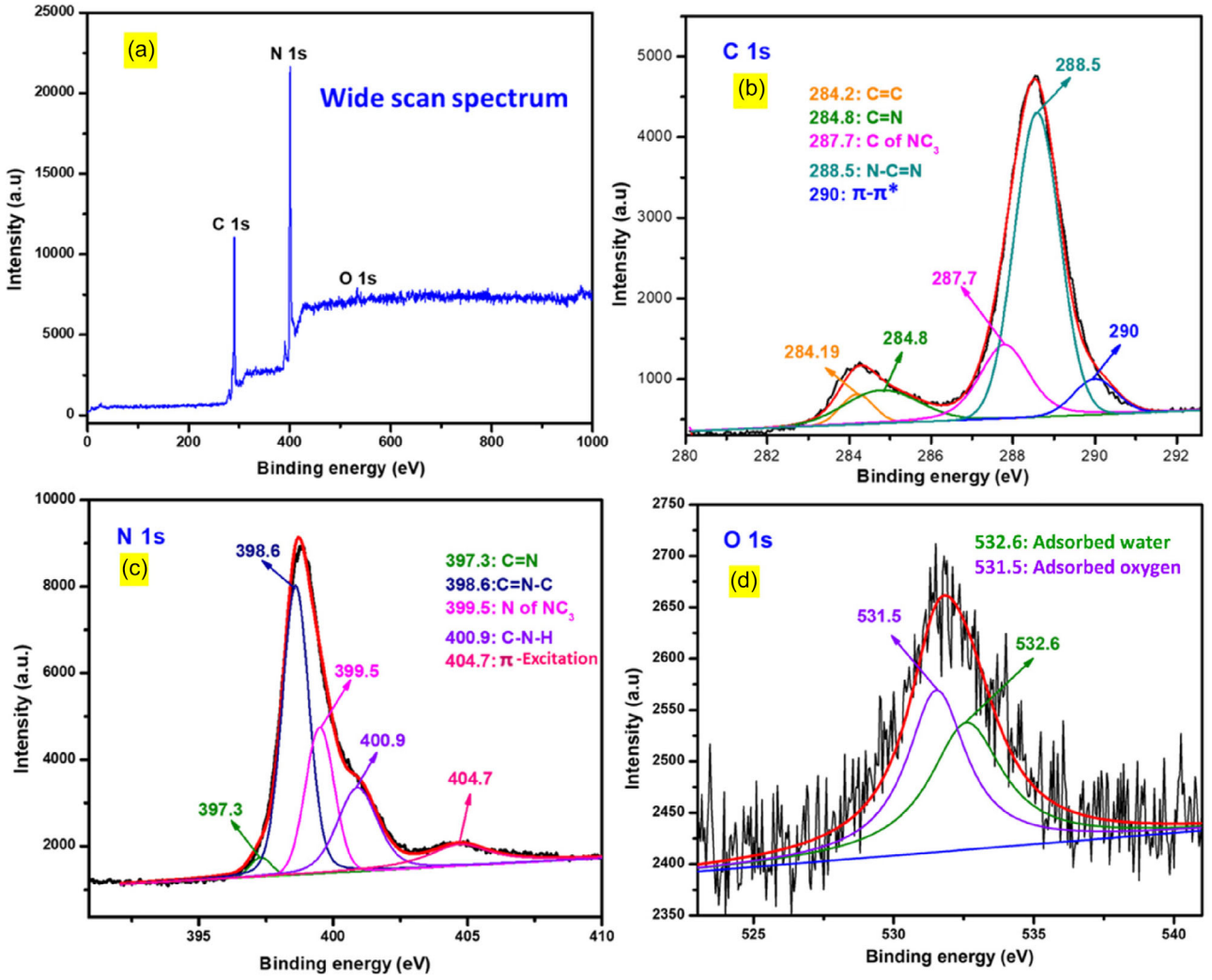

Figure 4. a) Wide scan XPS of g-C_3N_4/graphene, b) deconvoluted C 1*s* spectrum, c) deconvoluted N 1*s* spectrum, and d) deconvoluted O 1*s* spectrum.

with increased current density (Figure 5d). The specific capacitance of g-C_3N_4/graphene was computed at various current densities. An ultrahigh specific capacitance of 1415.7 F g^{-1} was obtained for the g-C_3N_4/graphene at a current density of 3 A g^{-1}. The specific capacitance varied to 1332.7, 1257.4, 1173.6, 1147.4, 1080.4, 1045.0, 1021.5, 819.8, 683.0, and 485.3 F g^{-1} with corresponding current densities of 4, 5, 6, 7, 8, 9, 10, 15, 20, and 30 A g^{-1}. The material features an excellent rate capability (72.1%) at the lower current density range of 3–10 A g^{-1}, as there are no massive alterations in the specific capacitance with varying current density, which can be due to the beneficial alignment of the component 2D materials, and mostly by the excellent electronic property of graphene rather than simple structural compensation.[18,75] The better rate capability also helps to achieve noticeable energy density.[76] The plot exhibiting the variation of specific capacitance with current density is shown in Figure 5e. Cyclic stability studies were also conducted in the three-electrode system, and g-C_3N_4/graphene retained 100% of the initial capacitance after 1500 CD runs (Figure 5f).

Hybrid materials exhibit merged charge storage mechanisms in supercapacitors, and therefore, it is essential to quantitatively distinguish these mechanisms to avoid misjudging their primary mode of charge storage, which gives better insight into the behavior of the system.[9] The charge storage mechanisms in energy storage systems can be either capacitive or Faradaic or a combination of these primary mechanisms.[77] In supercapacitors, most of the studies combine dominant capacitive charge storage with a minor Faradic charge storage characteristic in composites. The energy storage mechanism of g-C_3N_4/graphene is predicted here from the shape of CV and CD curves; whereas a more accurate and quantitative approach to resolve the energy storage mechanism is performed here by combining the theoretical models, Lindstrom method (Power law) and Dunn's method.[9] These methods efficiently figured out the percentage of capacitive and diffusive contributions to energy storage. The equations corresponding to both the Lindstrom method and Dunn's method, along with a detailed explanation, are given in the Supporting Information S3. In the Lindstrom method, log (*i*) against log (scan rate) was plotted from CVs recorded

Research Article
doi.org/10.1002/batt.202500499
Chemistry Europe
European Chemical Societies Publishing

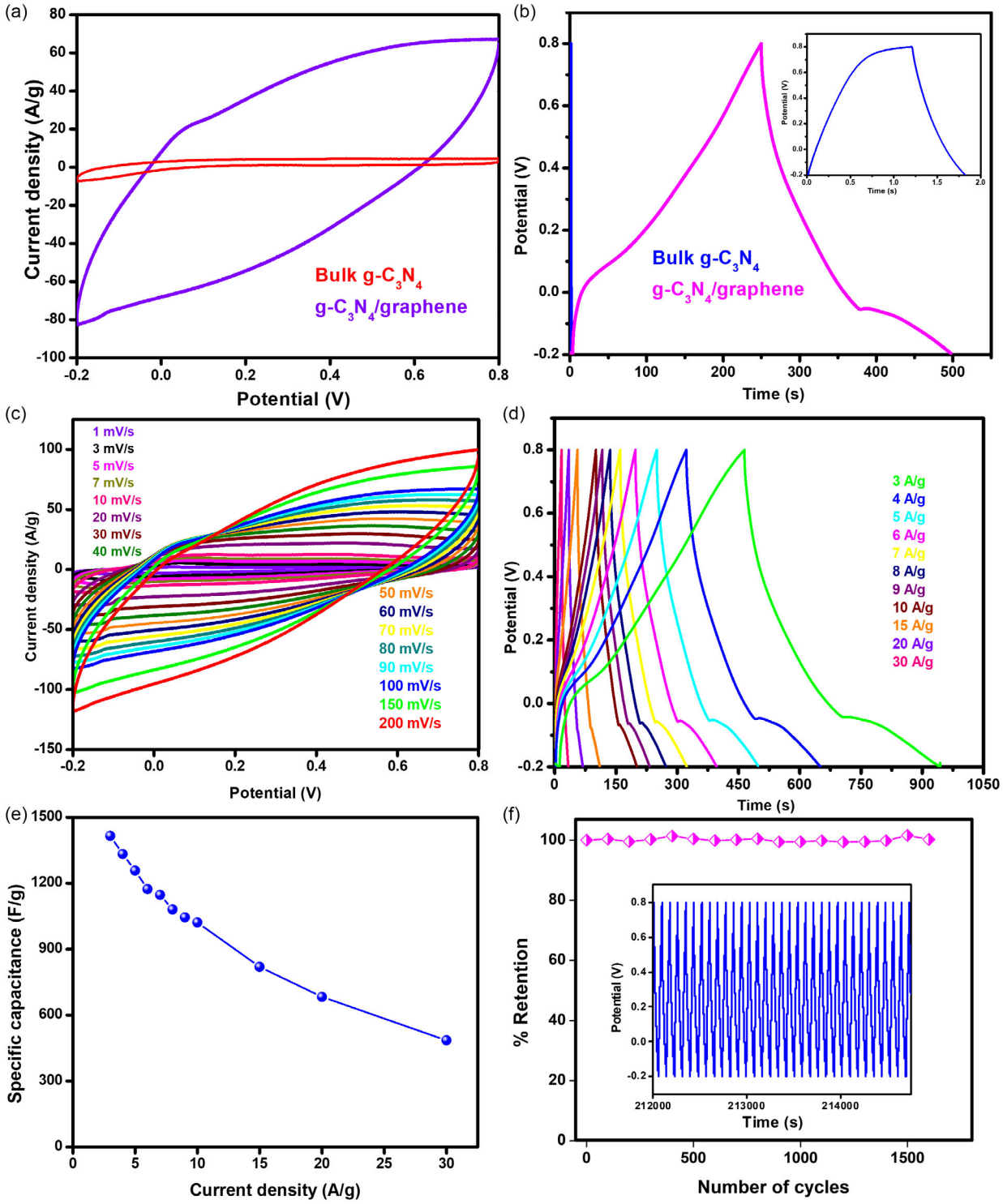

Figure 5. a) CVs of g-C_3N_4/graphene and bulk g-C_3N_4 at 100 mV s^{-1}, b) CD plots of g-C_3N_4/graphene and bulk g-C_3N_4 at 5 A/g, c) CVs of g-C_3N_4/graphene at different scan rates of 1–200 mV s^{-1}, d) CD plots of g-C_3N_4/graphene at different current densities from 2 to 30 A g^{-1}, e) Plot of specific capacitance with current density and f) Cyclic stability plot of g-C_3N_4/graphene.

at lower scan rates from 1 to 10 mV s^{-1} as given in **Figure 6**a. The plot is a straight line with a slope of 0.84, close to 1, promising a major capacitive contribution, adaptive to better supercapacitor performance.[77] Dunn's Equation (Equation 4), Supporting Information S3) more precisely differentiated capacitive and diffusive contributions by plotting $i/\sqrt{V}$ against $\sqrt{V}$. The slope and intercept of the plot gave constants *a* and *b* of Dunn's equation. The contributions from both capacitive and diffusive charge

Research Article
doi.org/10.1002/batt.202500499
Chemistry Europe
European Chemical Societies Publishing

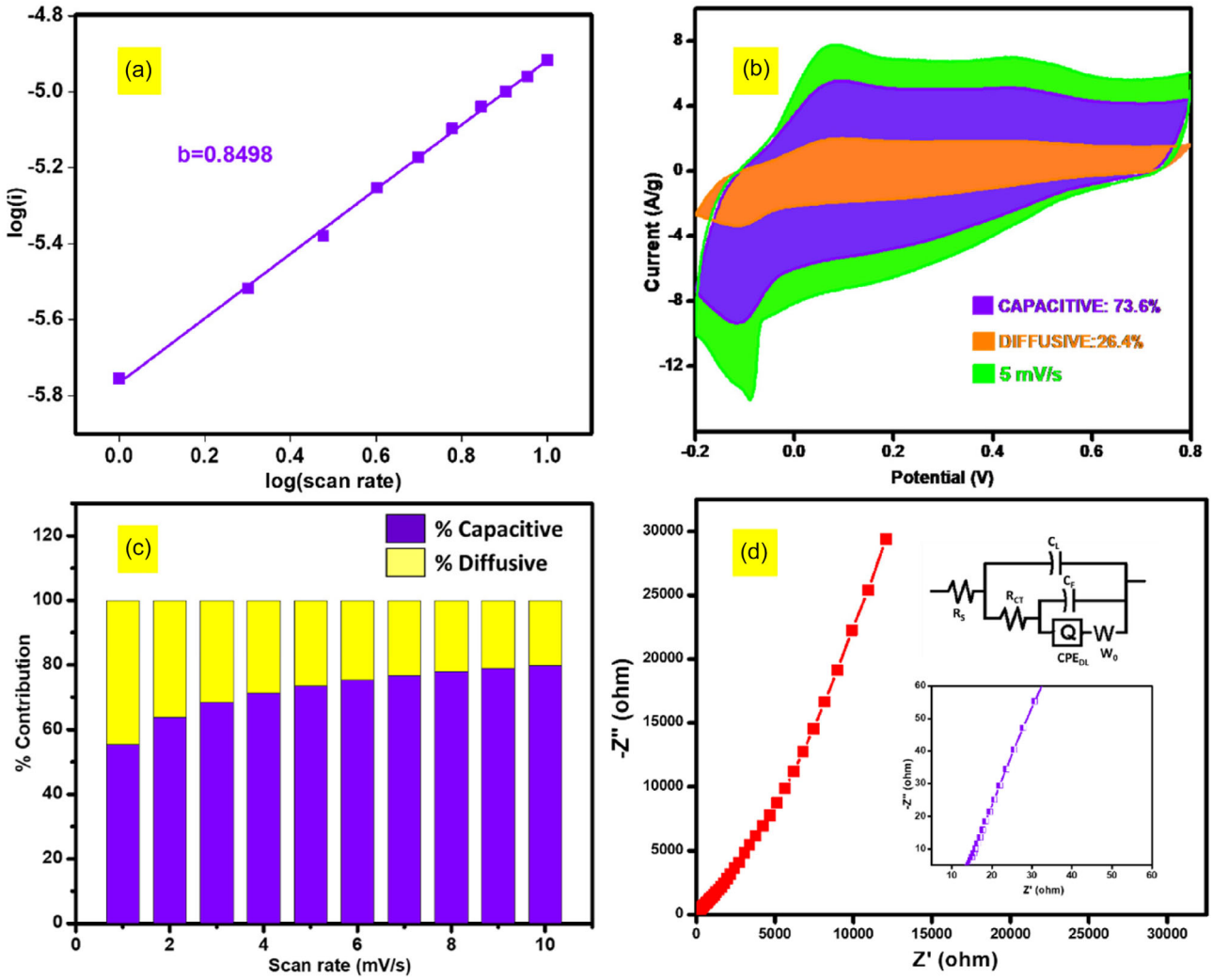

Figure 6. a) Power law plot of g-C_3N_4/graphene, b) Dunn's analysis of g-C_3N_4/graphene with percentage capacitive and diffusive contribution toward total capacitance at 5 mV s^{-1}, c) Plot of variation of percentage capacitive and percentage diffusive contributions with scan rates from 1 to 10 mV s^{-1}, and d) Nyquist plot of g-C_3N_4/graphene in the three-electrode system.

storage mechanisms are differentiated by Dunn's equation and plotted against potential, where from the area of the obtained plots, the charge storage mechanism is quantitatively distinguished.[9] The total capacitive and diffusive contribution is thus calculated for CVs obtained at different scan rates from 1 to 10 mV s^{-1}. Figure 6b shows the extracted diffusion-limited and capacitive charge storage contributions for 5 mV s^{-1}. At the intermediate investigated scan rate of 5 mV s^{-1}, g-C_3N_4/graphene exhibited a major capacitive contribution of 73.6% and a diffusive contribution of 26.4% indicating a distinct pseudocapacitance contribution to the energy storage attributed to the g-C_3N_4 present in the nanocomposite.

Since the total capacitive contribution is a combination of both double-layer capacitance from graphene and pseudocapacitance from g-C_3N_4, the total capacitive contribution is further resolved (explained in Supporting Information S3).[9,77]

A potential window $\Delta E^{\#}$ in the CV at the scan rate of 5 mV s^{-1}, where $i \propto v$, is selected, and by calculating the area under this region, the double-layer capacitance contribution is calculated (using Equations (7) and (8) in Supporting Information S3). The pseudocapacitance contribution is then calculated by subtracting the percentage double-layer capacitance contribution from the total capacitive contribution. The analysis reveals that pseudocapacitance accounts for 33.5% of the overall capacitive contribution, which is 73.6% of the total charge storage. Thus, the hybrid system has a merged energy storage mechanism with 26.4% diffusive contribution, 33.5% pseudocapacitive contribution, and 40.1% of pure double-layer capacitance. Further evaluation of the variation of capacitive and diffusive contributions with increasing scan rate (Figure 6c) indicates that, with the increase in scan rate, the percentage capacitive contribution kept on increasing as expected, and the percentage diffusive contribution continued to decrease mutually for scan rates ranging from 1 to 10 mV s^{-1}.

Electrochemical impedance spectroscopy (EIS) is a fundamental tool to analyze the overall resistive behavior of electrode

materials in supercapacitor studies.[78] The Nyquist plot of g-C_3N_4/graphene obtained from the EIS measurements and the correlated circuit diagram of resistive elements is given in Figure 6d. The Nyquist plot is a straight line inclined to the *Y*-axis in both the high and low frequency regions. The absence of a well-defined semicircle in the high-frequency region of the Nyquist plot indicates negligible charge transfer resistance.[79,80] The equivalent circuit consists of the elements R_S, R_{CT}, W_o, C_L, CPE_{DL}, and C_F. Even though the Nyquist plot of g-C_3N_4/graphene does not display a semicircle region, the R_{CT} component in the equivalent circuit arises from the deviations from ideal capacitive behavior due to the presence of pseudocapacitive g-C_3N_4 having a diffusion-controlled charge storage mechanism.[81,82] The intercept of the Nyquist plot with the real axis in the high-frequency region corresponds to the ohmic resistance or solution resistance (R_S) resulting from the resistance between the electrode and electrolyte, and it is found to be 12.26 Ω. Additionaly, there is charge transfer resistance represented as R_{CT} (10.26 Ω), and double layer capacitance C_L is present in series with the solution resistance and parallel with each other.[83] The central loop of the circuit contains elements W_o, CPE_{DL}, and C_F, which respectively represent Warburg impedance, constant phase element, and Faradaic capacitance. Warburg impedance is prominent at the low frequency region, and its inclination represents the lower diffusion limitation and hence a minimal resistance.[84]

Through various material characterization studies and electrochemical evaluations, the supercapacitor performance of g-C_3N_4/graphene electrode was assured, and thus a coin cell supercapacitor device was further fabricated with the g-C_3N_4/graphene to prove the real-sense applications.

2.3. Electrochemical Studies of Symmetric Coin Cell Supercapacitor

Here, carbon cloth was used as the current collector to fabricate the electrodes of a coin cell supercapacitor. Metal strips are the common current collectors in most of the commercial supercapacitors that need the quickest replacement to tune the supercapacitor fabrication in the future. The assembly inside the coin cell supercapacitor is depicted in the figure given in section S6 of the Supporting Information.

Electrochemical activity of the prepared coin cell was also assessed by CV, CD, and EIS studies. The maximum voltage of the device was optimized as 1 V, aiding CV studies, and the transition in its shape with diverging scan rates was also evaluated. **Figure 7**a shows the CVs recorded for the device at scan rates from 2 to 100 mV s^{-1}. The symmetrical quasi-rectangular shape of the CV curves indicates the good electrochemical capacitance behavior of the device, the area of which kept on increasing with increasing scan rates, implying stable performance. The CD curves of the device shown in Figure 7b are symmetric with negligible IR drop, highlighting the least possible internal resistance, which benefits excellent capacitive behavior of the g-C_3N_4/graphene electrodes.

The CD plots recorded over the range of 0.1 to 10 mA cm^{-2} displayed the highest capacitance of 222.3 mF cm^{-2} (168.3 F g^{-1}) at a current density of 0.1 mA cm^{-2}. The CD plots exhibited good rate capability in the range of 0.1–1 mA cm^{-2} (91.3%). The obtained specific capacitance values for the device versus current densities are plotted in Figure 7c. The cyclic stability evaluation results of the device are plotted in Figure 7d. After 10,000 CD cycles, the device showed improved performance (109.9%) compared to its initial state, indicating excellent activity and promising long-term usability. The hybrid material thus demonstrates the efficient inhibition of layer restacking common among graphene-based materials and thereby provides stable performance over continuous CD cycles. This performance also proves the efficient coin cell assembly, ensuring stable activity and the advantage of a well-coated electrode.

EIS of the device was recorded to evaluate the electron transfer processes, and it is provided with a suitable fitted circuit as given inside Figure 7e. In the Nyquist plot of the EIS, the high-frequency region features a semicircle due to the charge–transfer resistance endured within the device.[82] This semicircle in the high-frequency region, followed by another semicircle, indicates two distinct charge transfer resistances present within the system (as given in the inset).[82] However, the data for the fitted circuit declare the whole effect as minimal, supported by the least value for R_{CT} (0.42 Ω cm^2) due to the efficient conducting π-conjugation in the graphene with the undisturbed aromatic network leading to high conductivity. The low-frequency region consists of a straight line indicating a Warburg impedance with lower diffusion limitations as evident from the elements obtained from the fitted circuit.[84] The equivalent circuit constitutes the elements R_S, R_{CT}, R_L, C_L, CPE_{DL}, and W_o (with values 0.4294, 1.835, 8.009 Ω, 2.702E-5 F, 0.001742 sec^n, and 0.04646 $sec,^5$ respectively). The solution resistance R_S is the aggregated contribution from the resistance of the electrode–electrolyte interface and the respective individual contributions.[82] R_S is in series with C_L, R_{CT}, R_L, and W_o. Also, R_L is parallel to the constant phase element CPE_{DL}. The constant phase element stands for the double-layer capacitance prominent in graphene-based materials. The effect of diffusion-controlled charge storage properties, along with a major capacitive contribution, is also reflected in the EIS data because the contribution of R_{CT} is indicative of slightly deviated from ideal capacitive behavior. This is attributed to the pseudocapacitive nature offered by g-C_3N_4 in the hybrid material.[82] The EIS data altogether portray an easy ion diffusion and electron transport within the fabricated coin cell supercapacitor.

Rather than just stable performance, energy density and power density are the major parameters for evaluating the excellence of a supercapacitor over conventional batteries and capacitors. Here, the coin cell supercapacitor has delivered a remarkable highest energy density of 23.3 Wh kg^{-1} and a power density of 3885.3 W kg^{-1} (calculated using equations given in Supporting Information S4). The energy and power densities of the device with varying current densities are plotted in Figure 7f. The activity of the coin cell supercapacitor was compared with similar hybrid material-based supercapacitor devices from the literature and is given in **Table 1**, which clarifies the overall excellence of the

Research Article
doi.org/10.1002/batt.202500499
Chemistry Europe
European Chemical Societies Publishing

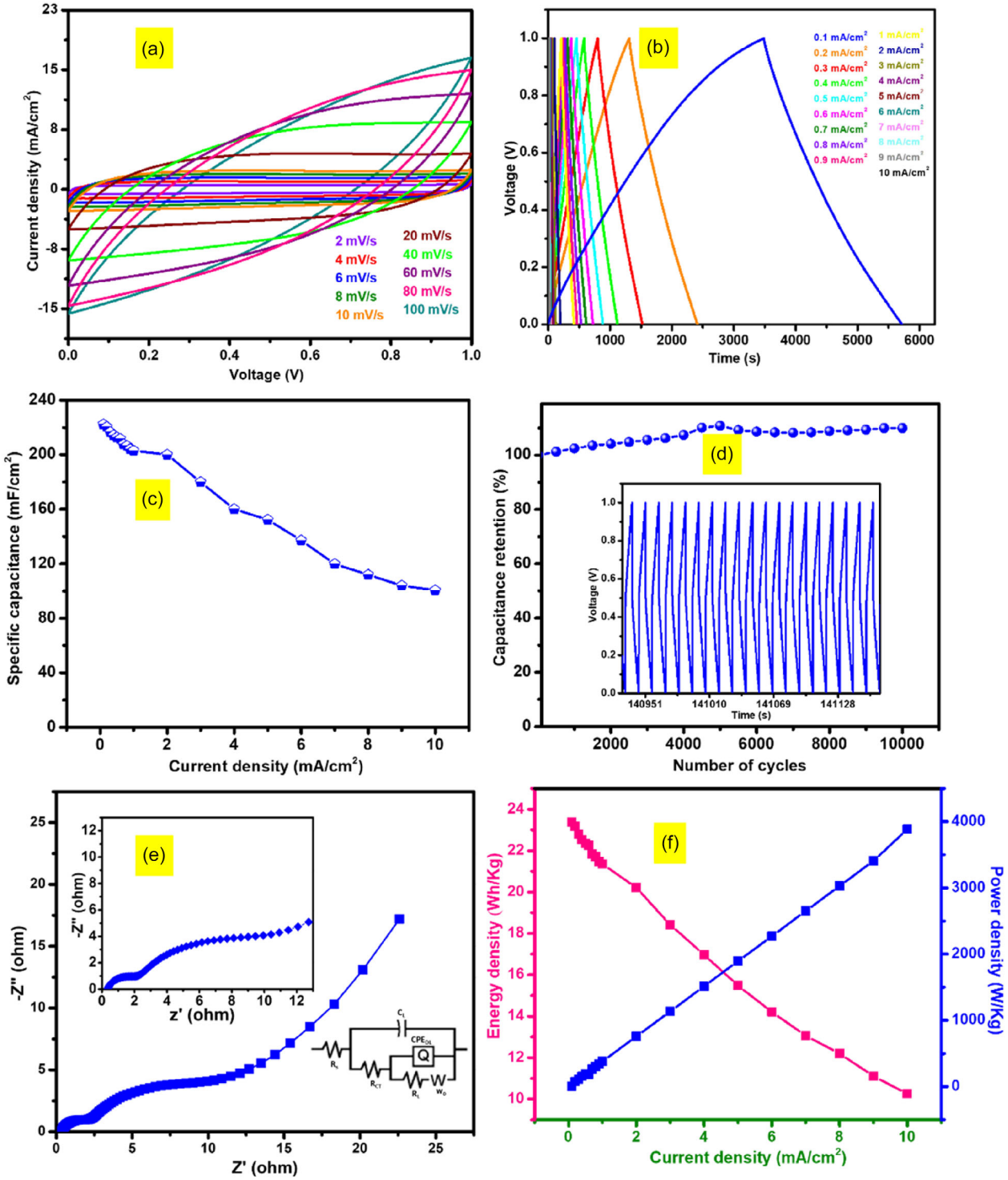

Figure 7. Electrochemical data of g-C_3N_4/graphene coin cell: a) CVs at different scan rates from 2 to 100 mV s^{-1}, b) CD plots at different current densities from 0.1 to 10 mA cm^{-2}, c) plot of areal capacitance with current density, d) cyclic stability of 10,000 CD cycles, e) Nyquist plot (fitted circuit and expanded region in the inset), and f) energy density v/s power density with varying current densities.

present g-C_3N_4/graphene, arising from the structural integration peculiar to the preparation process.

To verify the effect of continuous CD cycling on the structure, morphology, and properties of the nanocomposite, XRD analysis and FESEM imaging were performed on the sample after cyclic stability testing and compared with those of the electrode material before CD runs. As shown in **Figure 8**a, the XRD patterns exhibit no change in the peak positions, whereas there is a slight decrease in the intensity of the peaks corresponding to the (002) planes of both g-C_3N_4 and graphene, indicating further layer

Research Article
doi.org/10.1002/batt.202500499
Chemistry Europe
European Chemical Societies Publishing

Table 1. Comparison of the performance of the g-C_3N_4/graphene coin cell supercapacitor with similar two-electrode systems.

Composite	Electrolyte	Specific capacitance	Number of cycles	% Retention of capacitance	Energy density	Power density	Reference
GOOCN24[a)]	2 M KOH	170.7 F g^{-1}	10,000 (CV cycles)	87.9	14.93 Wh kg^{-1}	571.36 W kg^{-1}	[11]
rGO/g-C_3N_4/CF[b)]	PVA/KOH	61 mF cm^{-2}	5000	90	8.75 μWh cm^{-2}	0.45 mW cm^{-2}	[36]
C–C_3N_4@rGO[c)]	6 M KOH	379.7 F g^{-1}	10,000	85	52.7 Wh kg^{-1}	–	[87]
3D g-C_3N_4@G[d)]	$LiClO_4$	264 F g^{-1}	10,000	100	30 Wh kg^{-1}	4.0 kW kg^{-1}	[37]
g-C_3N_4/graphene	2 M H_2SO_4	222.3 mF/cm^{-2} (168.3 F g^{-1})	10,000	109.9	23.3 Wh kg^{-1}	3885.3 W kg^{-1}	This work

[a)]GOOCN24: 3D oxidized g-C_3N_4 functionalized graphene. [b)]rGO/g-C_3N_4/CF: rGO/g-C_3N_4 on carbon fiber. [c)]C–C_3N_4@rGO: carbon self-repairing g-C_3N_4 on rGO. [d)]3D g-C_3N_4@G: 3D graphitic carbon nitride functionalized graphene composite.

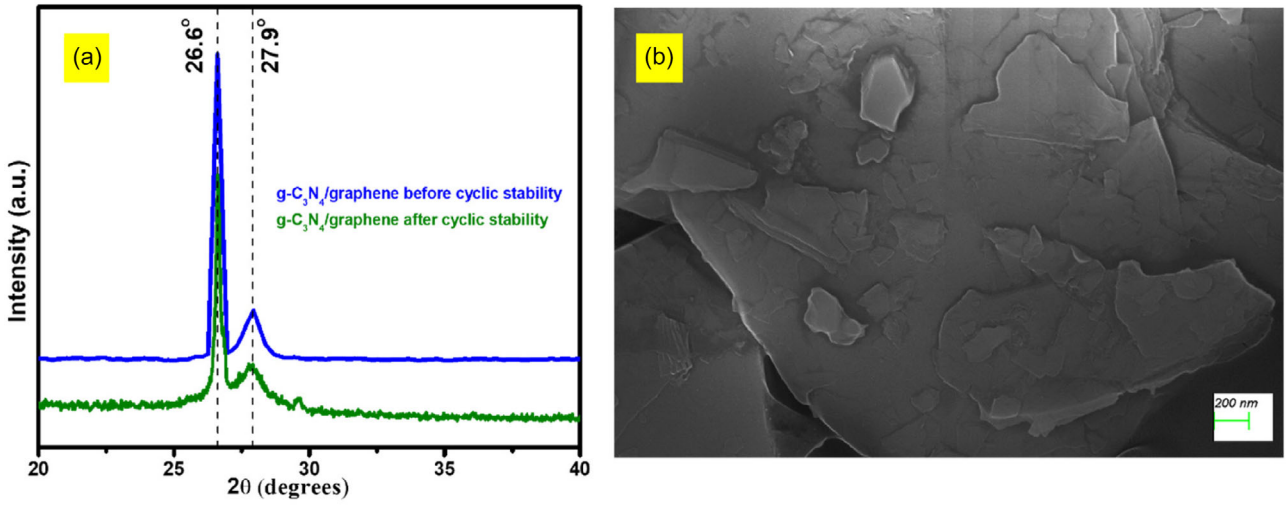

Figure 8. a) XRD patterns of g-C_3N_4/graphene before and after cyclic stability studies, and b) FESEM image of g-C_3N_4/graphene after cyclic stability investigation.

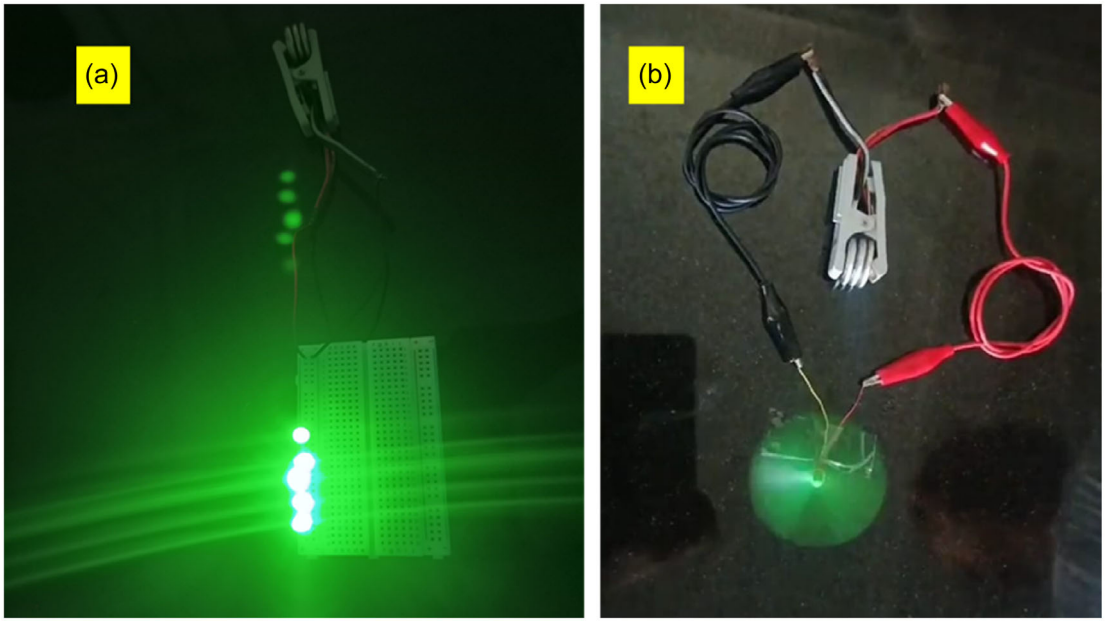

Figure 9. Three g-C_3N_4/graphene coin cells connected in series to power a) five LEDs and b) a mini motor attached mini-fan.

exfoliation, which may be due to the continuous insertion of electrolyte ions within the layers.[50,51] The results confirm the structural integrity and stability of the material. FESEM images of the nanocomposite after cyclic stability testing also reveal that the material's morphology shows no visible damage (Figure 8b).

Since the aqueous electrolyte-based supercapacitor devices possess the limitation of voltage expandable only up to 1.2 V, beyond which water splitting occurs, the required voltage can be attained by the series connections of the devices.[85,86] Here, we have combined three similar symmetric coin cells, which together provided a maximum of 3 V, and it was then charged to use for real-sense applications. The set of three devices, upon charging, lit five green LEDs showcasing its voltage retention and powered a mini motor attached mini-fan, highlighting its high-power density (**Figure 9**a,b). The video showing the working of the fan using the coin cell supercapacitor is included in the Supporting Information S7 (Video 1).

3. Conclusions

A simultaneous integration of top-down and bottom-up methods is employed here for the preparation of a metal-free g-C_3N_4/graphene hybrid material, aiding a mechanochemical exfoliation process using melamine as the milling media. The successful formation of the g-C_3N_4/graphene nanocomposite was confirmed using various analytical techniques, evaluating the structure and morphology. The viability of the g-C_3N_4/graphene in supercapacitor applications was initially evaluated by the three-electrode studies, where it delivered an ultrahigh specific capacitance of 1415.7 F g^{-1} at a current density of 3 A g^{-1}, owing to the excellent electronic conductivity of the graphene matrix and enlarged active surface area collectively contributed by the well-exfoliated 2D materials with synergistic properties. The effective implementation of the g-C_3N_4/graphene in practical applications was first evaluated by constructing a coin cell supercapacitor having a higher areal capacitance of 222.3 mF cm^{-2} and exceptional stability. The coin cell exhibited a performance enhancement to 109.9% of its initial value after 10,000 CD cycles, indicating the reasonable superiority of the supercapacitor device in energy storage applications. Additionally, the supercapacitor exhibited a remarkable energy density of 23.3 Wh kg^{-1} and the highest power density of 3885.3 W kg^{-1}, surpassing most of the reported g-C_3N_4/GO composites. The excellent performance validates the importance of combined 2D materials and in situ preparation in enhancing the energy storage capability for the next-generation supercapacitors. The practical applicability studied by lighting LEDs and powering a mini-fan verifies the material's potential for various energy storage applications.

4. Experimental Section

Preparation of g-C_3N_4/Graphene Hybrid Nanocomposite

g-C_3N_4/graphene was prepared by ball milling of graphite (Sigma Aldrich, CAS No: 7782-42-5) with melamine (Loba Chemie Pvt. Ltd.), followed by thermal treatment. In a typical procedure, about 1 g of graphite and 30 g of melamine were mixed and transferred to the mill along with a total of 200 g of stainless-steel balls. The container was tightly closed, and ball milling was performed for 30 h. After milling, the obtained mixture was transferred into a silica crucible, which was then tightly closed and calcined at 550 °C for 3 h in a muffle furnace. The same calcination procedure was repeated with melamine alone to prepare bulk g-C_3N_4.

Supercapacitor Performance Evaluation

A three-electrode setup was used to evaluate the supercapacitor performance of the g-C_3N_4/graphene nanocomposite and to compare it with bulk g-C_3N_4. For this study, an electrochemical cell, consisting of an Ag/AgCl reference electrode, a platinum wire counter electrode, and a glassy carbon electrode (GCE) coated with g-C_3N_4/graphene as the working electrode, was used. For g-C_3N_4/graphene to coat over the GCE, the material was well dispersed in a 1:1 v/v mixture of isopropyl alcohol (IPA, Nice chemicals Pvt. Ltd.) and water. Typically, g-C_3N_4/graphene, soot additive (Philips Carbon Black Ltd.), and polyvinyl alcohol (PVA, Loba Chemie Pvt. Ltd.) binder in the ratio 8:1:1 were dispersed in an IPA/water mixture. This dispersion was drop-casted onto the GCE surface and dried to obtain the g-C_3N_4/graphene-modified GCE. 1 M H_2SO_4 (Loba Chemie Pvt. Ltd.) was used as the electrolyte for the studies, and initial CV measurements were recorded using an electrochemical analyzer (CHI1210C, CH Instruments, USA). Galvanostatic CD studies and EIS measurements were performed in an electrochemical workstation (ZAHNER Zennium Pro 43,121). All the electrochemical measurements were taken in the potential range −0.2 to 0.8 V (1V). CV was recorded at different scan rates from 1 to 200 mV s^{-1}, and CD measurements were taken at different current densities from 2 to 30 A g^{-1}. Specific capacitance values at different current densities were determined using Equation (1) given in the supporting information S2. The EIS was carried out in the frequency range 0.1 kHz to 0.1 MHz, and the coulombic efficiency of the system was also recorded. Cyclic stability of the system was also studied by recording continuous CD cycles. Dunn's method was employed to calculate the percentage capacitive and diffusive contributions to the total capacitance (Supporting Information S3).

Symmetric Coin Cell Supercapacitor Fabrication and Performance Evaluation

A symmetric coin cell supercapacitor was fabricated using g-C_3N_4/graphene as the electrode material. Electrodes were prepared by drop coating g-C_3N_4/graphene dispersed in 1:1 IPA/water with graphite powder additive, and binder PVA in the ratio 7:2:1 (w/w) under ultrasonication onto carbon cloth (Shilpent Conductive Carbon Fiber, sheet resistance 3–5 Ohm sq^{-1}) of 13 mm diameter. The electrodes were then dried at 100 °C. A filter paper soaked in 2 M H_2SO_4 was used as the separator. The prepared electrodes and separator carrying the electrolyte were then assembled inside a coin cell case (CR2032) and carefully crimped with a coin cell crimping machine (STC-SF120, Shenzhen Tico Technology Co., Ltd.). The supercapacitor performance of the coin cell supercapacitor was also examined with CV, GCD, and EIS studies. The voltage was fixed at 1 V, and CV was recorded at different scan rates from 2 to 100 mV/s. From the CD curves, specific capacitance values at different current densities were also calculated. From the obtained data, the corresponding energy (E_D in Wh kg^{-1}) and power densities (P_D in W kg^{-1}) of the coin cell supercapacitor were also calculated using Equation (5) and (6) given in the Supporting Information S4.

Acknowledgements

H.V.P. acknowledges NSFDC for the NFSC research fellowship (grant no. NSFDC/E-81088). KSCSTE Thiruvananthapuram is also acknowledged for the research fellowship (for the period 03.03.2021 to 24.07.2023). Department of Physics, CUSAT, is acknowledged for FESEM analysis. Central Sophisticated Instrumentation Facility (CSIF), University of Calicut, is also acknowledged for FESEM analysis. CDST, SAIF Cochin, India, is acknowledged for XRD, FTIR, HRTEM, and TGA analysis. Indian Institute of Science Education and Research (IISER) Thiruvananthapuram is acknowledged for the XPS analysis. The authors acknowledge the PSG Institute of Advanced Studies (PSG IAS), Coimbatore, for Raman spectral analysis, and the Centre for Materials Characterization (CMC), National Institute of Technology (NIT), Calicut, for EDS mapping. The University of Calicut and SNGS College, Pattambi, is acknowledged for providing the facilities for carrying out the research work.

Conflict of Interest

The authors declare no conflict of interest.

Author Contributions

Haritha Valiyaveettil Padi: material preparation, characterization, electrochemical studies, coin cell supercapacitor fabrication, interpretation of data, and manuscript original drafting. **Binitha N. Narayanan**: scientific idea, supervision, conceptualization, resources, interpretation of data, funding acquisition, and manuscript- reviewing and editing. **Vijayasree Haridas**: material preparation, characterization, manuscript-reviewing and editing. All authors reviewed, edited, and approved the manuscript.

Data Availability Statement

The data that support the findings of this study are available from the corresponding author upon reasonable request.

Keywords: ball milling · electrode material · g-C_3N_4/graphene · metal-free · supercapacitor

[1] F. Dalir, M. S. Motlagh, K. Ashrafi, *J. Clean. Prod.* **2018**, *188*, 362.
[2] K. Mensah-Darkwa, C. Zequine, P. K. Kahol, R. K. Gupta, *Sustainability* **2019**, *11*, 414.
[3] S. Suriyakumar, P. Bhardwaj, A. N. Grace, A. M. Stephan, *Batter. Supercaps* **2021**, *4*, 571.
[4] M. I. A. A. Maksoud, R. A. Fahim, A. E. Shalan, M. Abd Elkodous, S. O. Olojede, A. I. Osman, C. Farrell, A. H. Al-Muhtaseb, A. S. Awed, A. H. Ashour, D. W. Rooney, *Environ. Chem. Lett.* **2021**, *19*, 375.
[5] L. Kong, C. Tang, H.-J. Peng, J.-Q. Huang, Q. Zhang, *SmartMat* **2020**, *1*, 1007.
[6] A. Afif, S. M. Rahman, A. Tasfiah Azad, J. Zaini, M. A. Islan, A. K. Azad, *J. Energy Storage* **2019**, *25*, 100852.
[7] J. Yu, Y. Wang, L. Shen, J. Liu, Z. Wang, S. Xu, H. M. Law, F. Ciucci, *Adv. Mater.* **2025**, *37*, 2417796.
[8] Q. Wu, T. He, Y. Zhang, J. Zhang, Z. Wang, Y. Liu, L. Zhao, Y. Wu, F. Ran, *J. Mater. Chem. A.* **2021**, *9*, 24094.
[9] T. Schoetz, L. W. Gordon, S. Ivanov, A. Bund, D. Mandler, R. J. Messinger, *Electrochim. Acta* **2022**, *412*, 140072.
[10] M. Michalska, J. Pavlovsky, E. Scholtzova, P. Skorna, V. Matejka, K. Bochenek, A. Jain, K. Chida, T. Yoshii, H. Nishihara, *Results Eng.* **2024**, *24*, 103109.
[11] R. Lin, Z. Li, D. I. Abou El Amaiem Amaiem, B. Zhang, D. J. L. Brett, G. He, I. P. Parkin, *J. Mater. Chem. A.* **2017**, *5*, 25545.
[12] D. P. Chatterjee, A. K. Nandi, *J. Mater. Chem. A.* **2021**, *9*, 15880.
[13] S. Patnaik, A. Behera, K. Parida, *Catal. Sci. Technol.* **2021**, *11*, 6018.
[14] M. F. El-Kady, Y. Shao, R. B. Kaner, *Nat. Rev. Mater.* **2016**, *1*, 16033.
[15] Y. Zhou, F. Guan, F. Zhao, Y. Shen, L. Bao, *Batter. Supercaps* **2023**, *6*, e202200536.
[16] Y. Huang, J. Liang, Y. Chen, *Small* **2012**, *8*, 1805.
[17] W. Luo, S. Chou, J. Wang, Y. Zhai, H. Liu, *Small* **2015**, *11*, 2817.
[18] J. Ph. Mensing, C. Poochai, S. Kerdpocha, C. Sriprachuabwong, A. Wisitsoraat, A. Tuantranont, *Adv. Nat. Sci. Nanosci. Nanotechnol.* **2017**, *8*, 033001.
[19] N. Cao, Y. Zhang, *J. Nanomater.* **2015**, *2015*, 168125.
[20] S. Rao, J. Upadhyay, K. Polychronopoulou, R. Umer, R. Das, *J. Compos. Sci.* **2018**, *2*, 25.
[21] B. Deng, Z. Liu, H. Peng, *Adv. Mater.* **2019**, *31*, 1800996.
[22] K. Krishnamoorthy, S. J. Kim, *J. Ind. Eng. Chem.* **2015**, *32*, 39.
[23] G. Huang, P. Jiang, X. Zhang, C. Zhou, J. Zhou, Y. Huang, P. Yang, L. Yang, X. Tian, Y. Hao, *Diam. Relat. Mater.* **2022**, *130*, 109438.
[24] J. Li, M. Östling, *Crystals* **2013**, *3*, 163.
[25] Y. Qu, X. Zhang, W. Lü, N. Yang, X. Jiang, *J. Mater. Sci.* **2020**, *55*, 16334.
[26] J. Cherusseri, D. Pandey, J. Thomas, *Batter. Supercaps* **2020**, *3*, 860.
[27] J. Safaei, N. Aida Mohamed, M. F. M. Noh, M. Fairuz Soh, N. Ahmad Ludin, M. Adib Ibrahim, W. N. R. W. Isahak, M. A. M. Teridi, *J. Mater. Chem. A* **2018**, *6*, 22346.
[28] A. Hayat, M. Sohail, A. El Jery, K. M. Al-Zaydi, K. F. Alshammari, J. Khan, H. Ali, Z. Ajmal, T. A. Taha, I. Ul Din, R. Altamimi, M. A. Hussein, Y. Al-Hadeethi, Y. Orooji, M. Z. Ansari, *Chem. Rec.* **2023**, *23*, e202200171.
[29] O. Iqbal, H. Ali, N. Li, A. I. Al-Sulami, K. F. Alshammari, H. S. M. Abd-Rabboh, Y. Al-Hadeethi, I. U. Din, A. I. Alharthi, R. Altamimi, A. Zada, Z. Wang, A. Hayat, M. Z. Ansari, *Mater. Today Phys.* **2023**, *34*, 101080.
[30] A. Hendaoui, A. Alshammari, *Materials* **2022**, *16*, 219.
[31] X. Yang, J. Peng, L. Zhao, H. Zhang, J. Li, P. Yu, Y. Fan, J. Wang, H. Liu, S. Dou, *Carbon Energy* **2024**, *6*, e490.
[32] M. Wuttke, Z. Liu, H. Lu, A. Narita, K. Müllen, *Batter. Supercaps* **2019**, *2*, 929.
[33] Y. Chen, C. Lu, *Carbon Neutraliz.* **2023**, *2*, 585.
[34] D. Liu, T. Van Tam, W. M. Choi, *RSC Adv.* **2022**, *12*, 3561.
[35] A. R. Sonkawade, S. S. Mahajan, A. R. Shelake, S. A. Ahir, M. R. Waikar, S. S. Sutar, R. G. Sonkawade, T. D. Dongale, *Int. J. Hydrog. Energy* **2024**, *87*, 1416.
[36] M. Ding, Y. Qu, X. Zhang, L. Duan, X. Li, W. Lü, *New J. Chem.* **2021**, *45*, 923.
[37] Q. Chen, Y. Zhao, X. Huang, N. Chen, L. Qu, *J. Mater. Chem. A.* **2015**, *3*, 6761.
[38] L. Shabnam, S. N. Faisal, V. C. Hoang, A. Martucci, V. G. Gomes, *J. Electroanal. Chem.* **2020**, *856*, 113503.
[39] K. Zhu, Y. Du, J. Liu, X. Fan, Z. Duan, G. Song, A. Meng, Z. Li, Q. Li, *J. Nanosci. Nanotechnol.* **2017**, *17*, 2515.
[40] Y. Zhao, J. Zhang, L. Qu, *ChemNanoMat* **2015**, *1*, 298.
[41] I.-Y. Jeon, S.-Y. Bae, J.-M. Seo, J.-B. Baek, *Adv. Funct. Mater.* **2015**, *25*, 6961.
[42] C. Lin, L. Yang, L. Ouyang, J. Liu, H. Wang, M. Zhu, *J. Alloys Compd.* **2017**, *728*, 578.
[43] S. Zhuang, E. S. Lee, L. Lei, B. B. Nunna, L. Kuang, W. Zhang, *Int. J. Energy Res.* **2016**, *40*, 2136.
[44] J. Orellana, E. Araya-Hermosilla, A. Pucci, R. Araya-Hermosilla, *Polymers* **2024**, *16*, 2273.
[45] R. Ranjan, R. S. Rai, V. Bajpai, *Diam. Relat. Mater.* **2020**, *110*, 108116.
[46] N. Xiao, D. Lau, W. Shi, J. Zhu, X. Dong, H. H. Hng, Q. Yan, *Carbon* **2013**, *57*, 184.
[47] V. León, M. Quintana, M. A. Herrero, J. L. G. Fierro, A. D. L. Hoz, M. Prato, E. Vázquez, *Chem. Commun.* **2011**, *47*, 10936.
[48] Y. Xue, H. Chen, J. Qu, L. Dai, *2D Mater.* **2015**, *2*, 044001.
[49] H. May, *J. Appl. Chem.* **1959**, *9*, 340.
[50] P. Dash, T. Dash, T. K. Rout, A. K. Sahu, S. K. Biswal, B. K. Mishra, *RSC Adv.* **2016**, *6*, 12657.
[51] P. Qiu, H. Chen, C. Xu, N. Zhou, F. Jiang, X. Wang, Y. Fu, *J. Mater. Chem. A.* **2015**, *3*, 24237.

[52] L. Chabib, Nursal, M. Miskam, N. H. Mohd Kaus, M. H. Shafie, M. Hamid, I. R. Saragi, I. Isnaeni, D. Amilia, I. B. Dalimunthe, H. Wijoyo, *Case Stud. Chem. Environ. Eng.* **2025**, *11*, 101057.
[53] S. C. Yan, Z. S. Li, Z. G. Zou, *Langmuir* **2009**, *25*, 10397.
[54] J. Tong, L. Zhang, F. Li, K. Wang, L. Han, S. Cao, *RSC Adv.* **2015**, *5*, 88149.
[55] C. Chuaicham, K. Sekar, Y. Xiong, V. Balakumar, Y. Mittraphab, K. Shimizu, B. Ohtani, I. Dabo, K. Sasaki, *Chem. Eng. J.* **2021**, *425*, 130502.
[56] H. Zou, X. Yan, J. Ren, X. Wu, Y. Dai, D. Sha, J. Pan, J. Liu, *J. Materiomics* **2015**, *1*, 340.
[57] J. Liang, C. Jing, J. Wang, Y. Men, *Molecules* **2021**, *26*, 7054.
[58] J. Tian, Q. Liu, A. M. Asiri, K. A. Alamry, X. Sun, *ChemSusChem* **2014**, *7*, 2125.
[59] Z. Junping, W. Zheng, T. ZhengFang, L. I. J. Yue, A. PengHang, Z. Mingli, A. Hongzhi, *Sci. Rep.* **2024**, *14*, 6350.
[60] V. Zólyomi, J. Koltai, J. Kürti, *Phys. Status Solidi B* **2011**, *248*, 2435.
[61] L. M. Malard, M. A. Pimenta, G. Dresselhaus, M. S. Dresselhaus, *Phys. Rep.* **2009**, *473*, 51.
[62] J. Chen, X. Deng, Y. Cui, J. Xie, L. Cui, G. Jin, Y. Yang, *Diam. Relat. Mater.* **2025**, *151*, 111818.
[63] D. Carboni, B. Lasio, V. Alzari, A. Mariani, D. Loche, M. F. Casula, L. Malfatti, P. Innocenzi, *Phys. Chem. Chem. Phys.* **2014**, *16*, 25809.
[64] J. Jiang, L. Ou-yang, L. Zhu, A. Zheng, J. Zou, X. Yi, H. Tang, *Carbon* **2014**, *80*, 213.
[65] X. Weng, H. Ye, W. Xie, M. Ying, H. Pan, M. Du, *Nanoscale Adv.* **2021**, *3*, 3900.
[66] Q. Zhang, J. Jing, Z. Chen, M. Sun, J. Li, Y. Li, L. Xu, *J. Mater. Sci. Mater. Electron.* **2019**, *30*, 15267.
[67] H. Senbill, A. Gangan, A. M. Saeed, M. E. Gad, J. Zeb, A. Fahmy, *Sci. Rep.* **2025**, *15*, 3334.
[68] A. N. Kadam, M. Moniruzzaman, S.-W. Lee, *Molecules* **2019**, *24*, 450.
[69] A. P. Dementjev, K. I. Maslakov, *Appl. Surf. Sci.* **2006**, *253*, 1095.
[70] T. Johnson, K. Wang, Q. H. Fan, A. Lee, *Discov. Nano* **2023**, *18*, 144.
[71] S. Yang, W. Zhou, C. Ge, X. Liu, Y. Fang, Z. Li, *RSC Adv.* **2013**, *3*, 5631.
[72] Z. Zhang, M. Zhang, F. Li, J. Tian, C. Yu, *Solid State Sci.* **2021**, *115*, 106605.
[73] L. Deng, J. Sun, J. Sun, X. Wang, T. Shen, R. Zhao, Y. Zhang, B. Wang, *Appl. Surf. Sci.* **2022**, *597*, 153586.
[74] C. Costentin, J.-M. Savéant, *Chem. Sci.* **2019**, *10*, 5656.
[75] A. Eftekhari, *J. Mater. Chem. A.* **2018**, *6*, 2866.
[76] B. Ramulu, J. A. Shaik, A. R. Mule, J. S. Yu, *Mater. Sci. Eng. R Rep.* **2024**, *160*, 100820.
[77] A. M. Afzal, N. Muzaffar, M. W. Iqbal, G. Dastgeer, A. Manzoor, M. Razaq, S. M. Wabaidur, E. A. Al-Ammar, S. M. Eldin, *J. Appl. Electrochem.* **2024**, *54*, 65.
[78] V. Sunil, B. Pal, I. Izwan Misnon, R. Jose, *Mater. Today Proc.* **2021**, *46*, 1588.
[79] A. Allison, H. A. Andreas, *J. Power Sources* **2019**, *426*, 93.
[80] B.-A. Mei, L. Pilon, *ECS Meet. Abstr.* **2017**, *MA2017-01*, 1468.
[81] J. Kang, J. Wen, S. H. Jayaram, A. Yu, X. Wang, *Electrochim. Acta* **2014**, *115*, 587.
[82] N. O. Laschuk, E. B. Easton, O. V. Zenkina, *RSC Adv.* **2021**, *11*, 27925.
[83] J. Luo, H. D. Jang, J. Huang, *ACS Nano* **2013**, *7*, 1464.
[84] F. Barzegar, A. Bello, D. Momodu, M. J. Madito, J. Dangbegnon, N. Manyala, *J. Power Sources* **2016**, *309*, 245.
[85] T. Guo, D. Zhou, L. Pang, S. Sun, T. Zhou, J. Su, *Small* **2022**, *18*, 2106360.
[86] A. Salisu, F. Hughson, R. Borah, X. Chen, A. Johns, A. Griesser, G. G. Andersson, T. Nann, R. V. Goreham, *Batter. Supercaps* **2025**, *8*, e202400305.
[87] Y. Ding, Y. Tang, L. Yang, Y. Zeng, J. Yuan, T. Liu, S. Zhang, C. Liu, S. Luo, *J. Mater. Chem. A.* **2016**, *4*, 14307.

Manuscript received: June 30, 2025
Revised manuscript received: August 17, 2025
Version of record online: